Arabian Journal of Chemistry 16 (2023) 105251

Contents lists available at ScienceDirect

Arabian Journal of Chemistry

journal homepage: www.sciencedirect.com

Original article

LED visible light assisted photo-oxidation of acetaminophen using one-step synthesis of Cu,Fe@g-C_3N_4 nanosheet – Activated persulfate system in aqueous solutions

Mahtab Alvandi [a,b], Heshmatollah Nourmoradi [a,b], Ali Nikoonahad [a,b], Ehsan Aghayani [c], Seyyed Abbas Mirzaee [a,b,*]

[a] Health and Environment Research Center, Ilam University of Medical Sciences, Ilam, Iran
[b] Department of Environmental Health Engineering, School of Public Health, Ilam University of Medical Sciences, Ilam, Iran
[c] Research Center for Environmental Contaminants (RCEC), Abadan University of Medical Sciences, Abadan, Iran

ARTICLE INFO

Article history:
Received 12 May 2023
Accepted 5 September 2023
Available online 9 September 2023

Keywords:
APAP
Persulfate
Hospital wastewater
Photocatalytic degradation
Cu,Fe@g-C_3N_4 nanosheet

ABSTRACT

In this work, the synthesis of Iron (Fe) and Copper (Cu) co-doped g-C_3N_4 was performed using the thermal decomposition of urea while iron nitrate and copper nitrate were used as dopant precursors. The fabricated catalyst (Fe-Cu@g-C_3N_4) was coupled with visible light and used for acetaminophen (APAP) degradation. The synthesized catalyst was characterized via several techniques including XRD, BET, BJH, SEM, TEM, EDX, EDS Dot mapping, DLS, and UV–Vis deflective reflectance spectroscopy. The performed characterization tests confirmed the successful synthesis of Fe-Cu co-doped g-C_3N_4 with high purity, nanosheet structure and high porosity (79.93 m^2/g). The complete APAP decomposition efficiency was achieved under optimal experimental conditions including pH of 11, catalyst dosage of 10 mg/L, PS dosage of 1 mM, and APAP concentration of 4 mg/L. The scavenging tests confirmed the major contribution of sulfate radicals and consequently, hydroxyl radicals for APAP removal. In addition, the kinetics of APAP degradation was studied and it revealed the pseudo first–order kinetics with 0.0698 min^{-1} rate constant. Finally, a plausible and tentative decomposition pathway was proposed for APAP degradation. The results of this study confirmed that the LED/catalyst (Cu, Fe@g-C_3N_4)/PS process could be an efficient and robust process for antibiotic-containing wastewater including hospital wastewater.

1. Introduction

Over the recent decades, there has been a growing global concern regarding the presence of emerging pharmaceuticals and personal care products (PPCPs) in aquatic environments. They have been found to have several detrimental impacts on both human health and environment (Mirzaee et al., 2021a; Hassani et al., 2020; Jaafarzadeh et al., 2019; Fakhri, Nematollahi et al. 2022; Qin et al., 2022;). Simultaneously, due to the rising demand for the prevention and treatment of human diseases, the widespread use of PPCPs has led to a significant increase in their production rate and therefore regarded as pseudo-persistent pollutants (Keerthanan et al., 2021).

Among the PPCPs, Acetaminophen (APAP), commonly known as paracetamol, is a widely used drug for its anti-inflammatory, antipyretic, and analgesic properties. However, it is also considered a persistent organic pollutant due to its high consumption rate, low absorption and degradation in the body (5–15%), and high solubility in water, resulting in the release of a significant amount of APAP into the environment every year (approximately 145,000 tons/year). The usual concentration of APAP in natural waters is in the range of ng/L to μg/L, but it can be higher in pharmaceutical wastewaters. For instance, water treatment plants in Bangkok and South Korea have reported APAP concentrations of 8.6 μg/L and 6.8 μg/L, respectively (Ying Li et al., 2012; Sim et al., 2010). APAP is toxic to aquatic life at concentrations greater than 1.8 μg/L,

* Corresponding author at: Health and Environment Research Center, Ilam University of Medical Sciences, Ilam, Iran.
E-mail addresses: mahtab.alvandisede@gmail.com (M. Alvandi), h.nourmoradi2004@gmail.com (H. Nourmoradi), nikoonahad_ali_n@yahoo.com (A. Nikoonahad), ehssanaghayani@gmail.com (E. Aghayani), Mirzaee.seyyed@gmail.com (S. Abbas Mirzaee).
Peer review under responsibility of King Saud University.

Production and hosting by Elsevier

https://doi.org/10.1016/j.arabjc.2023.105251
1878-5352/

emphasizing the need for effective treatment techniques to remove these contaminants from water sources (Noorimotlagh et al., 2016a; Kakavandi et al., 2019; Kim et al., 2007).

Nowadays, many studies have been conducted on the processes of removing persistent pharmaceuticals such as filtration and activated sludge process are effective but to a very low extent and methods such as absorption and coagulation-filtration are not able to remove these pollutants to acceptable extent (Y. Chen et al., 2016; D. Li et al., 2023; Songlin Wang et al., 2019). According to studies, advanced oxidation processes (AOPs) act as an efficient way to break down toxic organic pollutants into harmless inorganic salts, carbon dioxide, and water (Mirzaee, Jaafarzadeh et al. 2019b; Gholami, Abtahi et al. 2021;Duan et al., 2018; D. Li et al., 2019; Shuai Wang et al., 2021). AOPs by generating hydroxyl radicals (HO•) with high oxidation potential (1.8–––2.8 eV) are widely used to treat many organic pollutants (L. Chen et al., 2022; Ruppert et al., 1994; Zhou et al., 2022). Recently, AOPs based on sulfate radicals ($SO_4^{\bullet-}$) (SR-AOPs) have been introduced as a promising alternative to conventional methods for decomposing new pollutants. In the SR-AOPs, sulfate radicals ($SO_4^{\bullet-}$) can be generated by activating S_2O_8 or SO_5^{2-}, which have longer half-life periods, greater selectivity, and compatibility with a wider range of pH levels, and higher oxidation potential (2.5–––3.1 eV) compared to HO radicals. Moreover, the retention time of sulfate radicals (30–––40 μS) is longer than that of $HO^{\bullet}$ radicals (20 ns), providing more opportunities for attack and decomposition of target pollutant. Hence, the use of sulfate radicals in AOPs can yield better efficiency in removing pharmaceutical pollutants (Anipsitakis et al., 2004; Ghanbari et al., 2014; Lin et al., 2013).

Persulfate (PS) compounds need to be activated as sulfate radical precursors in SR-AOPs processes. There are various methods for its activation, which can be mentioned carbon-based materials, heat, microwave, ultrasonic irradiations, UV light, excited semiconductors and transition metals such as Fe^0, Fe^{2+}, Cu^{2+}, Co^{2+}, S, Na, K and Ag^+ (S. Hu et al., 2015, 2016, 2018; S. Hu, Chen, et al., 2017; Zhao et al., 2015). Among these methods, activation on carbon has been more economical, more compatible with the environment and has higher physicochemical capabilities (S. Hu, Qu, et al., 2017; J. Wang et al., 2018; Lei Yang et al., 2019). Graphitic carbon nitride (g-C_3N_4) is a polymer nanosheet composed of tris-triazine-based patterns with a C: N ratio of 3:4 and a small amount of hydrogen. As a new organic semiconductor material, it has the ability to absorb visible light, making it a popular choice in photocatalysis due to its high chemical stability and non-toxicity (Mehregan et al., 2022; Xiangxin Yang et al., 2008; Yuan et al., 2023; Zhu et al., 2018). However, factors such as low electrical conductivity and a reduced efficiency of photo-generated electron-hole pairs can limit its performance (Ong et al., 2015). To overcome these limitations, doping of transition metals has been identified as a viable solution. This process involves intentionally introducing foreign impurities into a semiconductor to manipulate its electronic structure, thereby controlling its conductive, optical, luminescent, magnetic, or other physical properties for targeted applications (J. Zhang et al., 2014).

Graphitic carbon nitride has an affinity to combine with metals, and metal salts mix uniformly with it. According to literature, addition of metal dopants would decrease the band gap energy, increase charge mobility, and increase catalytic activity (Al Mamari et al., 2023; Pan et al., 2021b). Studies have shown that Copper (Cu) could acts as an efficient and stable catalyst, and Cu placed on g-C_3N_4 has a strong catalytic activity for the removal of pharmaceutical pollutants in various waters/wastewaters (Pan et al., 2021b). in addition, copper-based catalysts perform well in a wide range of pH during the photocatalytic process and have shown high solubility in aqueous media (Ong et al., 2015; Pan et al., 2021a; Zou et al., 2014). Iron ions (Fe) are also highly compatible with the environment, but they need to be activated. One of the solutions to activate them is combining with g-C_3N_4, because of g-C_3N_4 contains heptazine rings with six nitrogen containing unpaired electrons and is able to combine with Fe (II) and Fe (III). Keeping this in mind, several studies show that iron is placed in a suitable form in the structure of g-C_3N_4 and has high efficiency in photocatalytic processes and shows good efficiency in a wide range of pH (Y. Feng et al., 2018; R. Li et al., 2020).

Therefore, in the present study, Cu,Fe@g-C_3N_4 nanocomposite was synthesized by one-step method, characterized using several techniques and its efficiency evaluated in order to activate PS as an oxidizer agent in the SR-AOPs to degrade APAP as an emerging pollutant in aqueous solution. The influence of the operational parameters in the degradation process was examined. Finally, the plausible decomposition pathways and the by-products and intermediates of APAP were determined during the obtained optimal experimental conditions.

2. Materials and methods

2.1. Materials

The raw materials used in this study included urea (CHN_2O), APAP was used in the form of white powder to make a stock solution, Ethanol and sodium persulfate ($Na_2S_2O_8$) were purchased from Samchun, Korea and iron nitrate Fe $(NO_3)_3$ and copper nitrate Cu $(NO_3)_2$ were purchased from Carlvarva, France. Ethanol was used to wash the synthesized nanoparticles and double distilled water was used as the process solvent. Methanol (HPLC grade, EtOH), water (HPLC grade) from Merck, Germany. Table.S1 depicted the structure and characteristics of APAP.

2.2. Catalysts synthesis

2.2.1. Synthesis of graphitic carbon nitride (g-C_3N_4)

In a typical synthesis procedure, 25 g of urea as a g-C_3N_4 precursor was ground well in an alumina crucible with a mortar. After obtaining a uniform mixture, heated in a furnace at 550 °C for 2 h. Then, to remove impurities of the obtained mixture, it was washed in several steps with an equal ratio of water and ethanol, then centrifuged for 10 min at 7000 rpm. The precipitate was separated and dried in an oven at 105 °C (D. Feng et al., 2017).

2.2.2. Synthesis of Cu,Fe@g-C_3N_4 nanocomposite

In this section, one-step synthesis method with less time consumption was applied. At first, 25 g of urea as a g-C_3N_4 precursor was ground well in an alumina crucible with a mortar, then 6 mM of iron (III) nitrate and 6 mM of copper (III) nitrate were added and was rubbed well again (In order to find the optimal required amount of iron and copper, the pre-test of different amounts of iron and copper were examined and the 6 mM of them regarding APAP removal was selected). After obtaining a uniform mixture, heated in a furnace at 550 °C for 2 h. Then, to remove impurities, it was washed in several steps with an equal ratio of water and ethanol and centrifuged for 10 min at 7000 rpm. The precipitate was separated and dried in an oven at 105 °C (Sarkar et al., 2020; Linhai Yang et al., 2021). The schematic of preparation process of Cu,Fe@g-C_3N_4 is shown in Fig. 1.

2.3. Characterization and analysis

The surface morphology and microstructure were observed using a GemniSEM500 scanning electron microscope (SEM) (Zeiss, Germany) and a JEM-F200 transmission electron microscope (TEM) (JEOL Ltd., Japan), respectively. The crystal phases of the photocat-

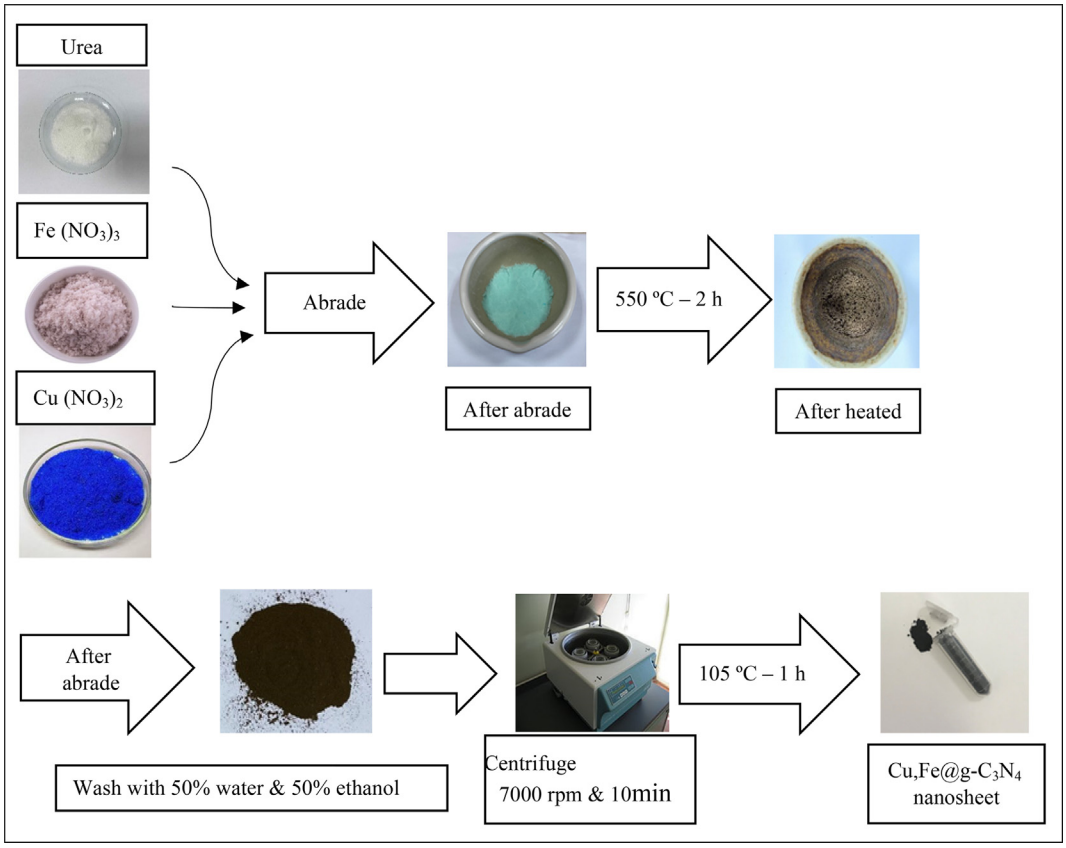

Fig. 1. The schematic of one-step synthesis of Cu,Fe@g-C_3N_4 nanosheet catalyst used in the photocatalytic removal of APAP.

alysts in this work were determined by X-ray diffraction (XRD) pattern using Co kα radiation for 2θ scan between 10 and 90°. Fourier transform infrared spectra (FT-IR) of as-prepared samples were recorded using KBr disk method in the range of 400 – 4000 cm^{-1} on a Tensor 27 (Bruker, Germany) infrared spectrometer to explore the chemical nature of the samples. Energy dispersive X-ray (EDX) was used for the elemental analysis of the catalyst. Pore size distribution and specific surface area of as-prepared samples were determined using BJH model and Brunauer-Emmett-Teller (BET) method using BELSORP mini II device (Microtrac MRB, USA). The UV–vis diffuse reflectance spectra (UV–vis DRS) of the samples are obtained using a Shimadzu UV-3600 spectrometer (Shimadzu, Japan) by using $BaSO_4$ as a reference. The concentration of APAP was determined by a high-performance liquid chromatography (HPLC) with a 250 mm × 4.6 mm Hypersil BDS C18 5 µm column. The temperature of column was set at 25 °C for APAP, the mobile phase was consisted of ethanol and ultrapure water, with a volume ratio of 70:30 and the flow rate of 1 mL/min. A diode array detector with a detection wavelength of 244 nm was used (LOD = 0.016 µg/L and LOQ = 0.05 µg/L). Total organic carbon (TOC) values were analyzed by TOC analyzer (Shimadzu, Japan, TOC-V CPN).

2.4. The APAP removal experiments

To prepare the APAP solution, the given amount of APAP was dissolved in deionized water. A stock solution of sodium persulfate was also made at a concentration of 10 mM. In the next step, 50 mL of the APAP solution with a concentration of 4 mg/L was placed into a 100 mL flask, and a specific amount of PS/ Fe,Cu@g-C_3N_4 was added. The pH of the solution was adjusted to different levels between 2 and 11. The flask containing the sample was then placed in a simple hand-made photocatalytic reactor, and exposed to an LED lamp with a wavelength of 400 nm (12 W). The remaining APAP concentration was measured at specific intervals. To quench the samples before measuring APAP concentration, ethanol was added to the solution. Moreover, sodium nitrite was used as active species scavenger in order to analyze TOC of final sample in the optimal condition.

3. Results and discussion

3.1. Structural and morphological studies

In order to investigate the crystal structure of pure carbon nitride and carbon nitride samples anchored with Fe and Cu atoms, X-ray diffraction analysis was used. As can be seen in Fig. 2, the peaks at 13.08 and 27.48°correspond to the crystal planes of the repeating s-triazine structural parts within the plane (100) and the layered aggregation of the p-conjugate planes (002), respectively (Ma et al., 2019). In the results obtained from the samples doped with Fe, Cu or both Fe and Cu atoms, no peak associated with Fe or Cu atoms is observed, which indicates the good performance of these atoms in the structure of carbon nitride nanosheet (Dong et al., 2017; Ma et al., 2019). Also, considering the small amount of these atoms in the structure of the synthesized nanocatalyst, this result was expected and is in good agreement with similar researches (Xiaoyu Yang et al., 2019). With the addition of Fe and Cu atoms to the carbon nitride nanoplate structure, the intensity of the characteristic peak of carbon nitride has decreased, which indicates a decrease in the amount of crystal formation due to the prevention of Fe and Cu atoms from forming a dense polymer structure and breaking the layer structure and reducing the size of crystal particles (Z. Li et al., 2016). This result was evaluated using Debby Scherrer's relation ($D = K\lambda/\beta\cos\theta$) and for sam-

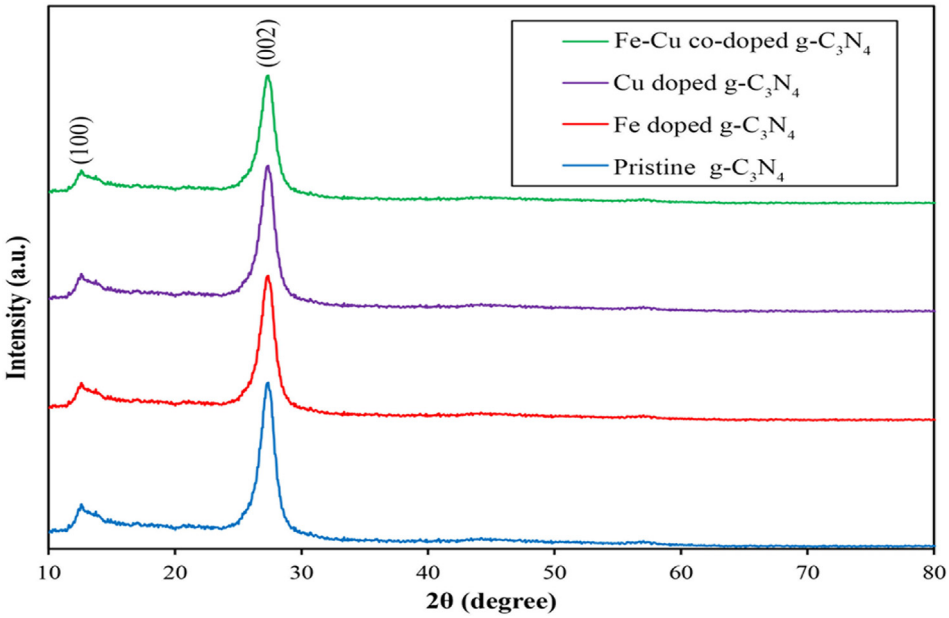

Fig. 2. XRD patterns of synthesized g-C_3N_4, Fe@g-C_3N_4, Cu@g-C_3N_4 and Fe, Cu@g-C_3N_4 nanocatalyst used in the photocatalytic process of APAP.

ples of g-C_3N_4 and Fe doped g-C_3N_4 and Cu doped g-C_3N_4 and Fe-Cu doped g-C_3N_4 the crystal sizes were 17.9, 15.4, 15.8, and 13.5 nm was obtained respectively. In addition, the partial movement (by 0.2°) of the characteristic peak of carbon nitride to a higher angle and the decrease of this characteristic peak can be due to the placement of Fe and Cu atoms next to nitrogen atoms and between carbon nitride layers and reducing the distance between be superficial (Adekoya et al., 2017). In addition, materials with poor crystal structure usually have more defects in their structure, which can trap a large amount of electrons and increase the rate of separation of produced electrons and holes. At the same time, the reduction of the interfacial distance facilitates the transport of carriers between the crystal layers. All these consequences are beneficial for improving the photocatalytic activity (Ma et al., 2019). Fig. 3**A** shows the nitrogen adsorption/desorption isotherms of synthesized g-C_3N_4 and Fe-Cu doped g-C_3N_4 catalysts. Based on results depicted in Fig. 3**A**, all samples were identified as type IV isotherm with overlap of the H_3 residual ring at a relative pressure between 0.2 and 0.9, indicating the *meso*-structural nature of the prepared nanocomposite. Also, the specific surface area of g-C_3N_4 and Fe-Cu doped g-C_3N_4 were 61.361 and 79.93 m^2/g, respectively. The results showed that the specific surface area of the g-C_3N_4 catalyst increased with the addition of Fe and Cu atoms, because Fe and Cu, as impurities, hinder the adhesion of g-C_3N_4 sheets and lead to an increase in the number of sheets (Ghanbari et al., 2021; Pan et al., 2021b). Therefore, the value of the specific surface area of the impurity sample is increased compared to the pure sample. Pore size distribution was investigated using BJH analysis. According to the Fig. 3**B**, the distribution of the diameter of the main pores of the samples in the range of mesoporous and macroporous materials was based on the IUPAC classification, which is consistent with the results obtained from the nitrogen absorption/desorption analysis (Ghane et al., 2020).

The morphology of the as-prepared samples was analyzed using both FESEM and TEM techniques. The micrographs of g-C_3N_4 and Fe-Cu doped g-C_3N_4 samples along with their corresponding EDAX

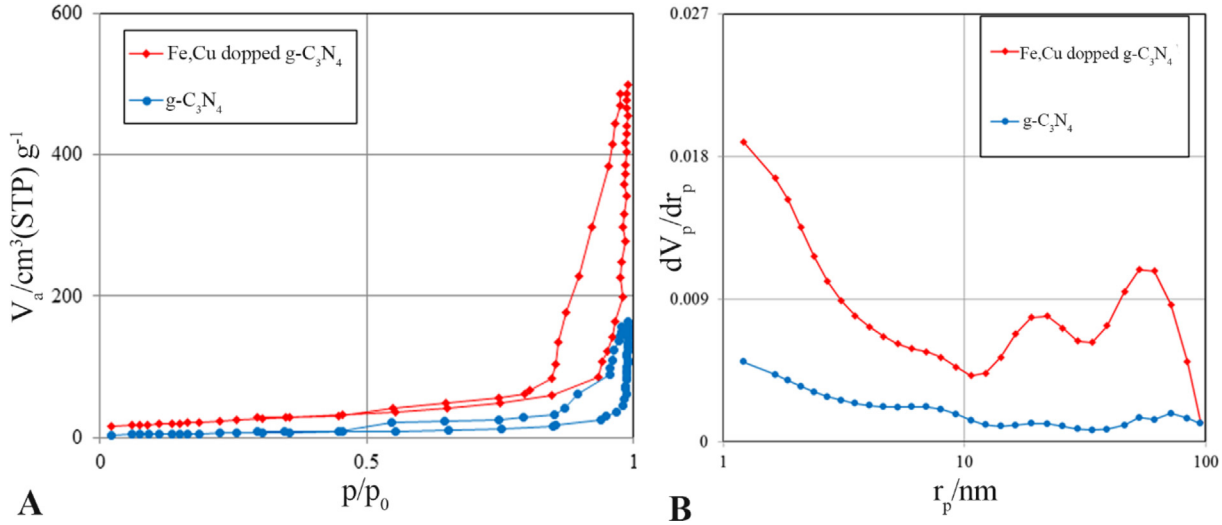

Fig. 3. (A) BET analysis (Nitrogen adsorption/desorption isotherms), and (B) BJH analysis of synthesized g-C3N4 and Fe-Cu@g-C_3N_4.

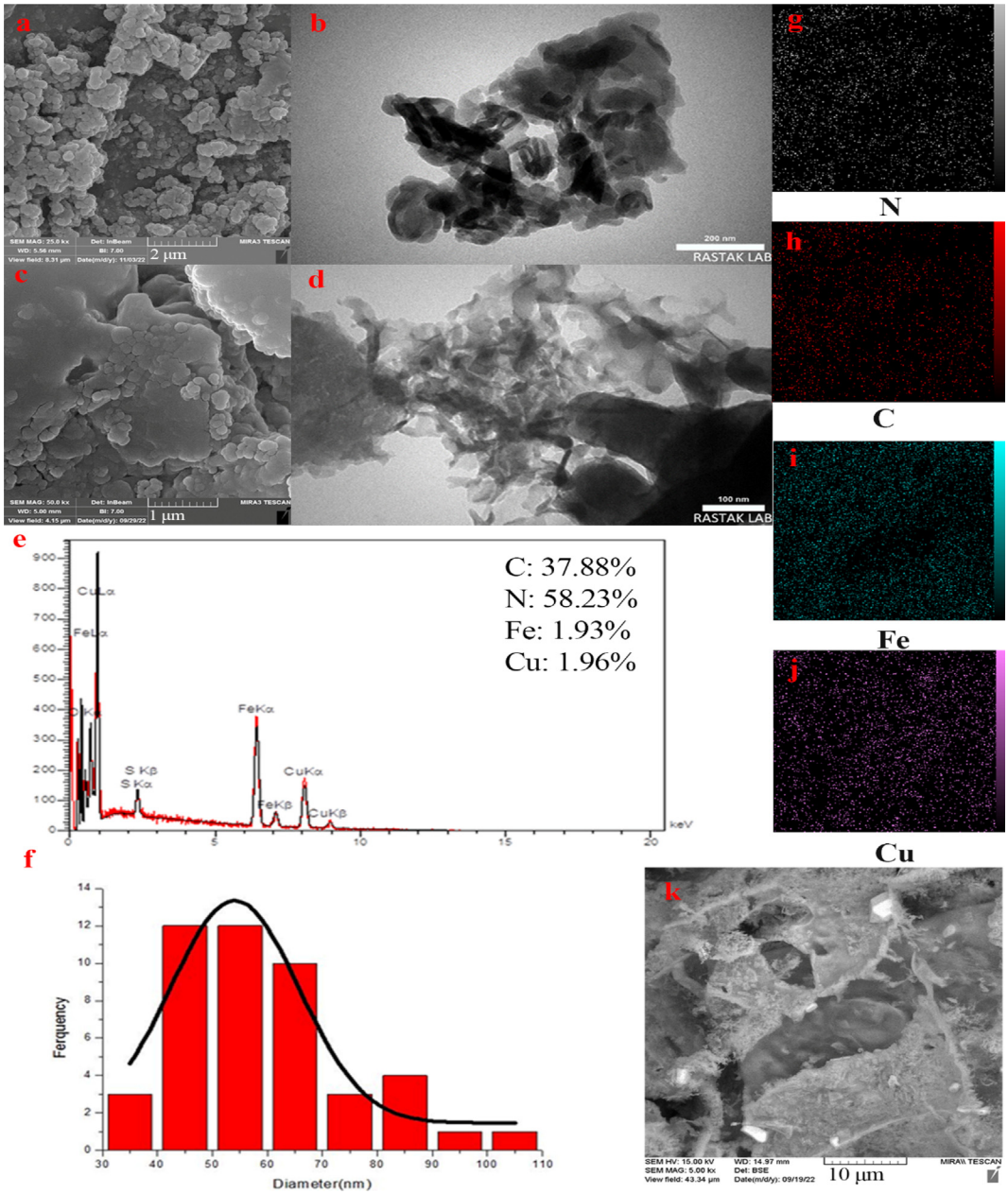

Fig. 4. FESEM and TEM micrographs of g-C_3N_4 (a and b) and Fe-Cu@g-C_3N_4 (c and d); EDAX analysis of Fe-Cu@g-C_3N_4 (e); DLS analysis for particle size distribution analysis of Fe-Cu@g-C_3N_4 (f); EDS Dot mapping of N (g), C (h), Cu (i), Fe (j), and SEM of the scanned area (k).

diagrams are presented in Fig. 4 **(a-e)** and SEM of the scanned area in Fig. 4 **(k)**. The micrographs of the catalysts show pseudo-plate morphology of g-C_3N_4 nanoparticles. This confirms that the addition of Fe and Cu did not change the morphology of g-C_3N_4. The FESEM images of g-C_3N_4 and Fe-Cu doped g-C_3N_4 displayed planar shapes of g-C_3N_4 and more porosity in the Fe-Cu doped g-C_3N_4 sample. This could be due to the addition of Cu and Fe atoms to the g-C_3N_4 structure, which leads to penetration and an increase in the distance between the sheets (J. Hu et al., 2016). These atoms are attributed to the distance between the sheets. The EDAX analysis confirms the high purity of the prepared catalysts, and the particle size distribution of the final sample indicates successful synthesis of nano-sized samples. Moreover, the average size distribution of the samples decreases with the addition of Fe and Cu atoms. These results are in agreement with those obtained from XRD analysis and the Scherrer equation, indicating successful synthesis of nano-sized samples and a decrease in average size distribution with the addition of impurities (N and Cu) (K. Li et al., 2015).

EDS dot mapping of Fe-Cu doped g-C_3N_4 nanocomposite provided in Fig. 4 **g-j**, which shows that all elements are completely uniformly distributed on the catalyst surface and all doped elements and g-C_3N_4 are optimally combined during the synthesis process (Liu et al., 2017).

UV–Vis Deflective Reflectance Spectroscopy analysis was performed to measure the amount of activation energy required to induce electrons and create holes in the valence layer and transfer electrons to the conduction layer of the catalyst. Based on previous studies, the reported Band-gap Energy for pure g-C_3N_4 sample is equal to 2.73 eV. In this study, Fe and Cu elements have been embedded to the composition as dopant materials (J. Hu et al., 2016; Pan et al., 2021b). The purpose of this work was to create

intermediate energy levels between the valence and conduction layers of g-C_3N_4 in order to increase the catalytic activity of g-C_3N_4. As shown in the Fig. 5, the band-gap energy of the Fe-Cu doped g-C_3N_4 catalyst has decreased to about 2.3 eV, which indicates the better performance of this catalyst in the visible light range (Bajiri et al., 2021).

3.2. APAP removal by PS/ Fe,Cu@g-C_3N_4/ LED

3.2.1. The effect of operating parameters on APAP degradation

The initial pH value has been introduced as an effective factor in the photocatalytic removal process. The initial pH value can significantly affect the degradation process by catalyst clumping, pollutant ionic state changing, and catalyst surface charge changing. In this regards, finding the optimal value of this factor plays a significant role in improving the catalytic removal process. The pH values are 2, 5, 7, 9, and 11, the pollutant concentration is 4 mg/L, the PS concentration is 1 mmol/L, and the catalyst concentration is 40 mg/L in order to find the optimal initial pH value of the case was evaluated. As can be seen in the Fig. 6**A,** the reaction efficiency increased dramatically from 20.28% to 100% by increasing the initial pH value from 3 to 11. This phenomenon is due to the increase of hydroxyl radical in the reaction medium **Eqs. (1) to (3)** (Yukun Li et al., 2022). Also, the absence of nitrate and carbonate ions in the reaction environment and the lack of consumption of electrons produced in the photocatalytic process to produce weak carbonate and nitrate radicals increases the production of hydrogen peroxide and hydroxyl radicals **Eqs. (4) to (6)** (L. Zhang et al., 2022).

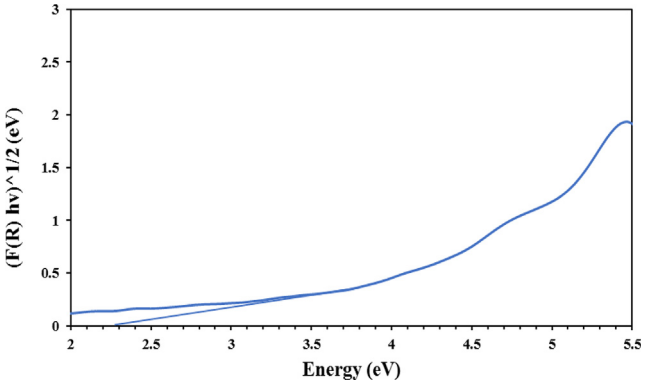

Fig. 5. UV–Vis Reflectance Spectroscopic analysis of Fe, Cu@g-C3N4 catalyst.

$$HO^{\cdot} + H^{+} + e^{-} \rightarrow H_2O \quad (1)$$

$$SO_4^{\cdot -} + H^{+} + e^{-} \rightarrow HSO_4^{\cdot -} \quad (2)$$

$$SO_4^{\cdot -} + HO^{-} \rightarrow SO_4^{2-} + HO \quad (3)$$

$$HO^{\cdot} + HO^{\cdot} \rightarrow H_2O_2 \quad (4)$$

$$HSO_5^{-} + e^{-} \rightarrow SO_4^{\cdot -} + OH^{-} \quad (5)$$

$$HSO_5^{-} + e^{-} \rightarrow SO_4^{2-} + OH^{\cdot} \quad (6)$$

The amount of catalyst in the process plays a vital role in the photocatalytic decomposition process.

The effect of different amounts of catalyst (0-–100 mg/L) was evaluated for the removal of APAP. As shown in the Fig. 6**B**, the efficiency of APAP removal from 61.71% after 60 min using 5 mg/L of catalyst to 100% APAP removal after 5 min using 60 mg/L of cata-

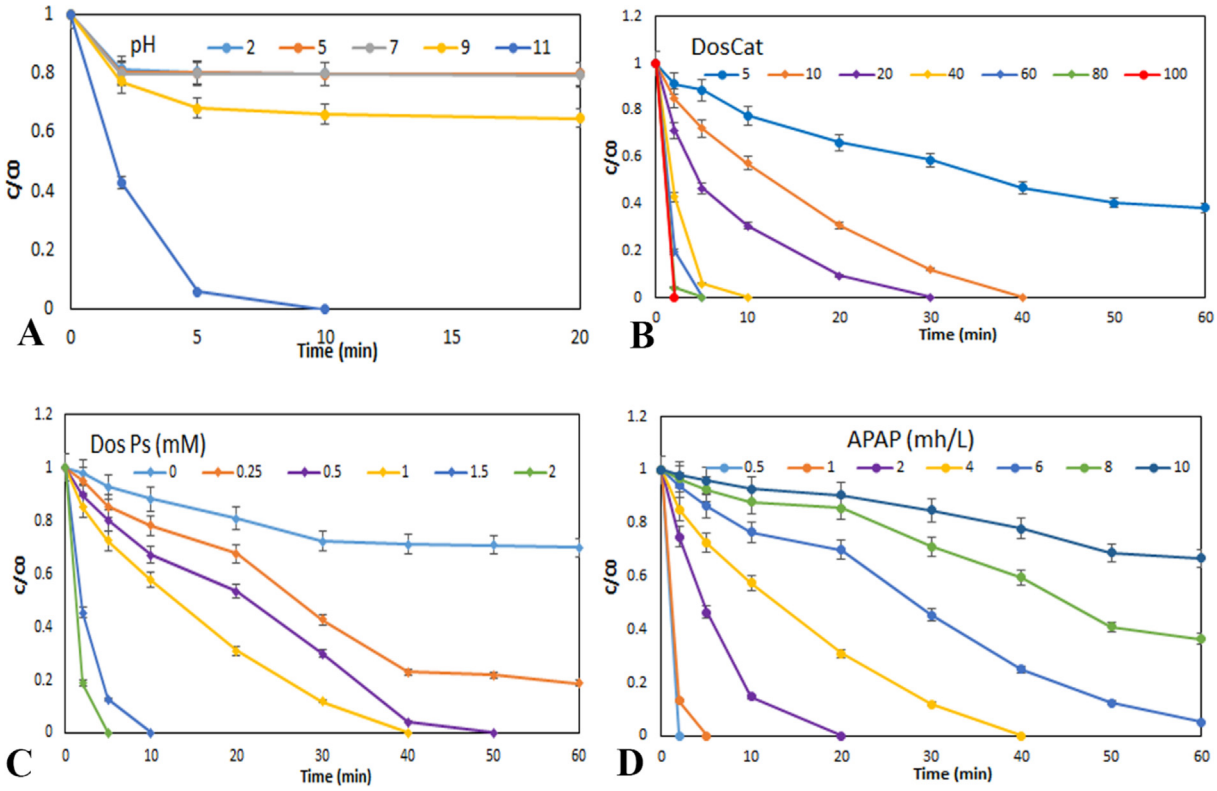

Fig. 6. Evaluation of effect of different (A) initial pH on the photocatalytic process of APAP removal (PS = 1 mM, Fe,Cu@g-C_3N_4 = 40 mg/L, APAP = 4 mg/L); (B) catalyst dosage at PH = 11, PS = 1 mM and APAP = 4 mg/L; (C) PS dosage at pH = 11, Fe,Cu@g-C_3N_4 = 10 mg/L and APAP = 4 mg/L; (D) APAP concentration at pH = 11, Fe,Cu@g-C_3N_4 = 10 mg/L and PS = 1 mM on the photocatalytic APAP degradation reaction.

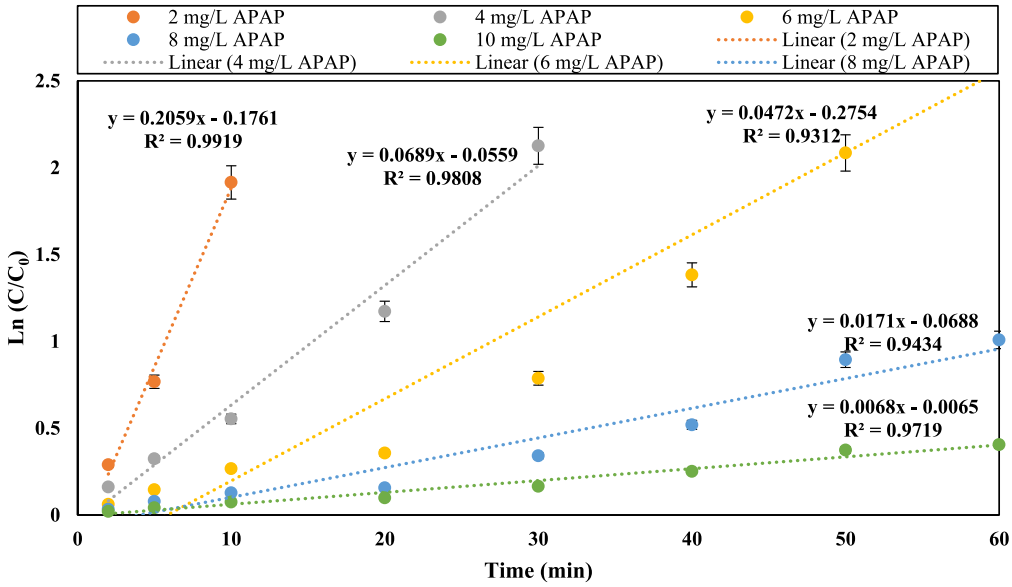

Fig. 7. Linear regression kinetic study of the photocatalytic removal process of APAP from 0 to 60 min.

lyst is reached. The increase in the removal of APAP is accompanied by the increase in the amount of catalyst in the reaction medium due to the increase in the specific surface of the catalyst and the increase in the number of active sites and the increase in the production of electron-hole pairs. Also, the increase of active sites increases the absorption of APAP molecules and side products, which increases the efficiency of the catalyst and further removes APAP from the environment. On the other hand, the increase in electron production accelerates the production of hydrogen peroxide and hydroxyl radicals, which themselves accelerate the removal of APAP from the reaction environment. In addition, in case of using high amounts of catalyst, the risk of clumping and destruction of the catalyst, as well as excessive turbidity of the environment and obstruction of light penetration, will cause a significant reduction in removal efficiency (Shi et al., 2022). Based on the results obtained, the catalyst amount of 10 mg/L was chosen as the optimal amount because with this amount of catalyst, 4 mg/L of APAP can be completely removed in 40 min.

The effect of different concentrations of PS on the removal rate of APAP from the aqueous environment is shown in Fig. 6**C.** By increasing the amount of PS from 0.25 mmol/L to 2 mmol/L, the amount of APAP removal increased dramatically, so that the removal time of APAP went from 60 min for a concentration of 0.25 mmol/L to 5 min for a concentration of 2 mmol/L has arrived. By increasing the concentration of PS, the rate of degradation of APAP increases, which is due to the increase in the amount of sulfate radicals produced by PS (Noorimotlagh et al., 2023b). Considering the importance of optimizing the removal process, the concentration of 1 mmol/L PS was considered as the optimal concentration. It should be noted that above PS, the active sites of the catalyst are limited for the activation of all PS molecules **Eqs. (7) and (8)** (Han et al., 2020), and the sulfate radicals themselves cause the consumption of sulfate radicals in an inefficient way according to **Eqs. (9) and (10)** (Tan et al., 2017).

$$SO_4^{\cdot -} + SO_4^{\cdot -} \rightarrow S_2O_8^{2-} \quad (7)$$

$$SO_4^{\cdot -} + HO^{\cdot} \rightarrow HSO_4^{-} + \tfrac{1}{2}\, O_2 \quad (8)$$

$$HSO_5^{-} + SO_4^{\cdot -} \rightarrow SO_4^{2-} + SO_5^{\cdot -} + H^{+} \quad (9)$$

$$HSO_5^{-} + HO^{\cdot} \rightarrow SO_5^{\cdot -} + H_2O \quad (10)$$

The effect of different initial concentrations of APAP (from 0.5 to 10 mg/L) was evaluated. By increasing the initial concentration of APAP from 0.5 to 10 mg/L, the duration of APAP removal increased dramatically, so that for the sample containing 10 mg, after 60 min, only 33.29% of APAP removal was obtained under optimal operating conditions. As shown in Fig. 6**D**, for the sample containing 4 mg/L of APAP, it was completely removed after 40 min. The increase in removal time and reduction in the removal efficiency of APAP at high concentrations can be due to the production of numerous intermediates that are obtained from the breakdown process of APAP. Also, due to the constant amount of catalyst, the amount of active species that is produced is limited and cannot remove high amounts of APAP (Takdastan et al., 2018). In addition, increasing the concentration of APAP plays a significant role in occupying active surface sites and deactivating the catalyst. It should be noted that in cases of high concentration of APAP, some of the emitted light photons are absorbed by APAP molecules and intermediate substances and the energy loss increases (Hayati, Isari, et al., 2020).

Table 1
Comparison of degradation efficiency of APAP reported in similar studies.

Reference	Process	Experimental Conditions	Removal rate %
(Kohantorabi et al., 2022)	Mn-doped g-C_3N_4 composite to activate PMS	15 min with initial pH 6.5, 0.8 g/L of PMS and 200 mg/L of catalyst of 0.5-MnCN	100
	Co-implanting of TiO_2 and liquid-phase-delaminated g-C_3N_4	0.6 g/L of TGCN (60:10:30) at pH = 9.0 within 120 min reaction	100
(Hassani et al., 2020)	PMS activation by $CoFe_2O_4$/ mpg-C_3N_4 nanocomposite	pH = 7.0, PMS = 1.5 mM, 40 mg/L CF/MCN and 25 min reaction time	92
Current study	one-step synthesis of Cu,Fe@g-C_3N_4 nanosheet to activate persulfate	pH = 11, Fe,Cu@g-C_3N_4 = 10 mg/L, PS = 1 mM and APAP = 4 mg/L in 40 min	100

In order to check the performance of each component of the APAP removal reaction, the performance of control reactions provided in Fig. 7. As shown, in the processes of photolysis (without PS), photolysis (without catalyst) and adsorption reaction of APAP (without presence of light), the APAP removal were obtained 20.1%, 18.5% and 6.2%, respectively, which indicates the inability of these reactions to completely remove APAP. By adding g-C_3N_4 catalyst to the reaction mixture, the removal efficiency of APAP pollutant reached 32%. By adding Cu and Fe dopants to the structure of g-C_3N_4 nanosheet, a significant increase in efficiency has occurred and the removal rate of APAP has reached 61.5% and 57.2%, which shows the positive effect of adding these elements to the catalyst structure. This increase is due to the reduction of the energy band and the reduction of the energy required to excite the electron and transfer this electron to the conduction layer (Hayati, Khodabakhshi, et al., 2020). By adding Fe and Cu atoms to the g-C_3N_4 structure simultaneously, the energy band has experienced a significant decrease, and more electrons have been excited with

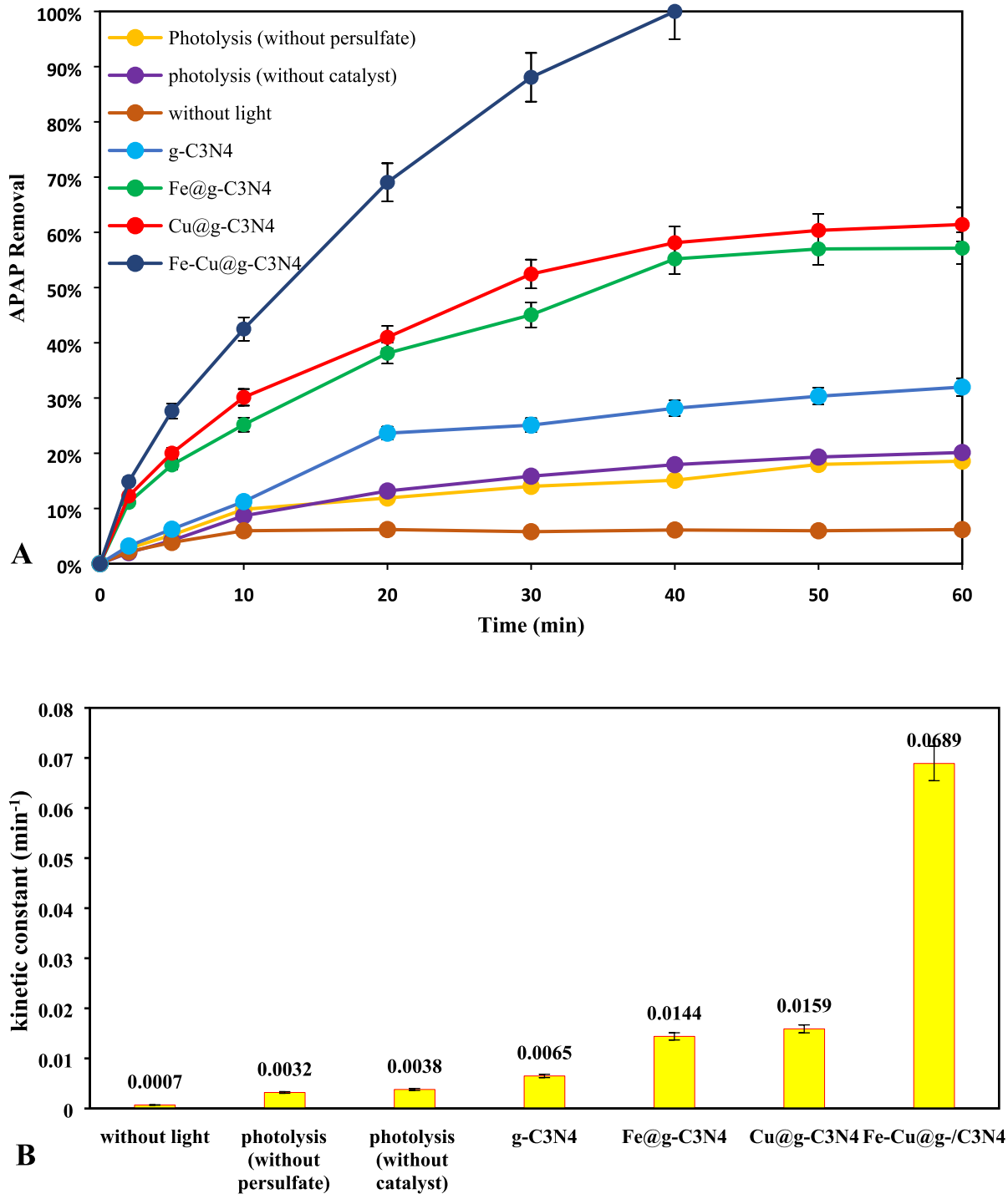

Fig. 8. (A) Performance analysis of different processes, and (B) kinetic constant for photocatalytic APAP removal under optimal degradation condition (pH = 11, PS = 1 mM and Catalysts = 10 mg/L, APAP = 4 mg/L).

less energy, and more wavelengths of visible light have been used to excite electrons. Table 1 shows comparison of degradation efficiency of APAP from similar reported studies. As can be seen at Table 1, the obtained results of the present work was in accordance with the similar studies.

3.2.2. The kinetic study of APAP removal by PS/Fe,Cu@g-C_3N_4 /LED system

The Langmuir-Hinshelwood kinetic (LHK) model, which is an important model for heterogeneous catalytic processes, was used to investigate the photocatalytic degradation kinetics of APAP with the PS/ Fe,Cu@g-C_3N_4/ LED process carried out in this research (Chang et al., 2017). The LHK equation can be expressed as follows:

$$r = -\frac{dC}{dt} = \frac{k_r K_{ad} C}{K_{ad} C + 1} \quad (11)$$

In **Eq. (11),** C is the initial concentration of the pollutant (mol), k_r is the reaction constant (mol/min), r is the reaction constant (mol/min), t is the reaction time, K_{ad} is the constant coefficient of pollutant absorption on the catalyst surface (per mol). In this research, each pollutant concentration and adsorption constant coefficient on the catalyst surface are very small, in other words, the value of $K_{ad}C$ is much smaller than one. Therefore, the **Eq. (12)** can be simplified to the first-order kinetic equation (Hayati, Isari, et al., 2020):

$$Ln\left(\frac{C_t}{C_0}\right) = -k_r K_{ad} t = -K_{app} \quad (12)$$

In **Eq. (12)**, C_0 is the initial pollutant concentration, C_t is the pollutant concentration at time t, and K_{app} is the reaction constant (per min).

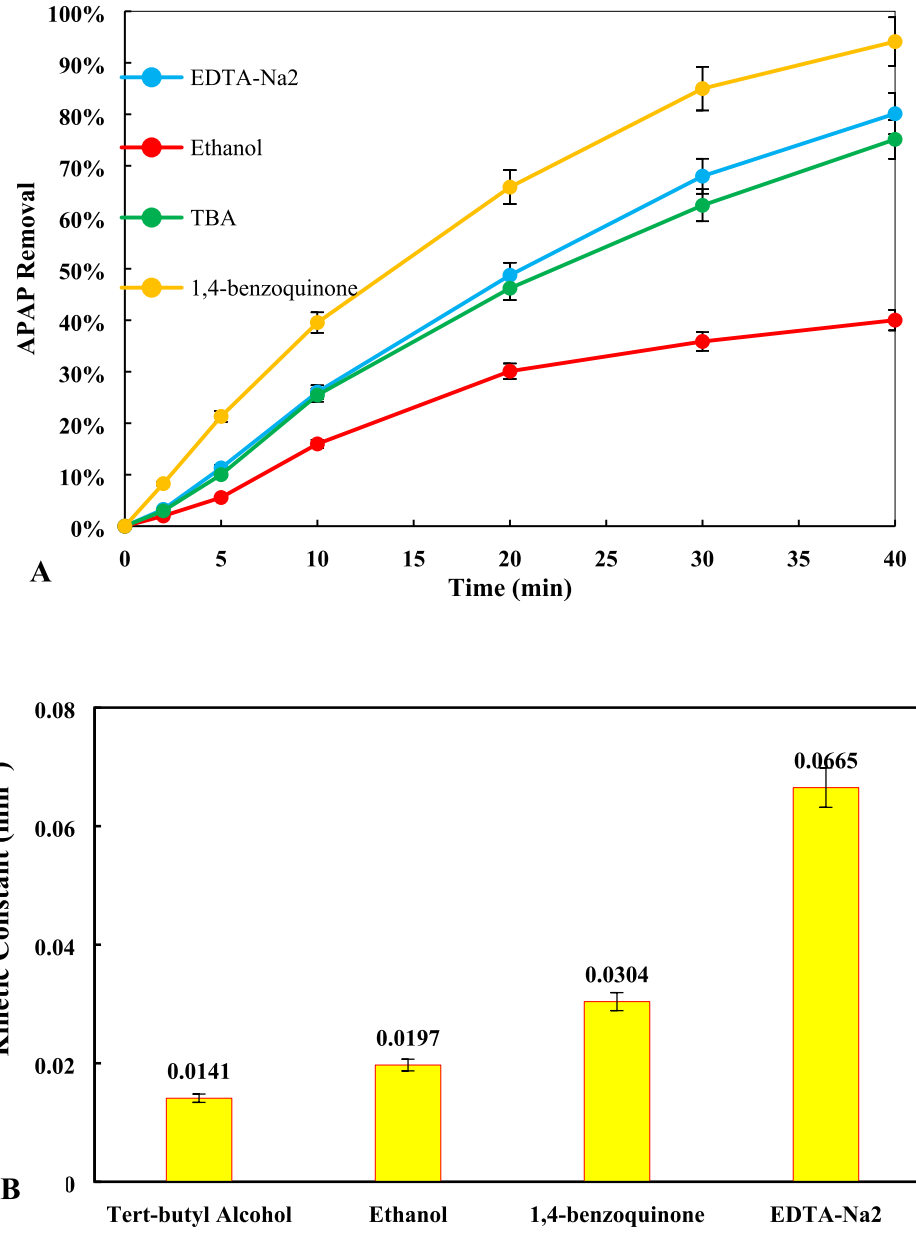

Fig. 9. (A) The role of active species, and (B) kinetic constant of effect of active species in the photocatalytic degradation of APAP (pH = 11, PS = 1 mM and Fe,Cu@g-C_3N_4 = 10 mg/L).

The linear form of the concentration–time equation can be used to ensure a fit between calculations and actual pollutant removal data. Specifically, the fit can be obtained by plotting Ln (C_t/C_0) versus time. Fig. 11 shows that the linear regression number (R^2- greater than 0.9) is very accurate and confirms the consistency of the data on the removal of APAP from the aqueous environment. Increasing the initial concentration of APAP has caused a gradual decrease in the reaction rate. On the other hand, the high value of the reaction constant shows the ability of the catalyst-light system (PS/Fe, Cu@g-C_3N_4/LED) to remove the APAP pollutant from the aqueous environment. Moreover, the kinetics of control experiments is provided in Fig. 8 for comparison of performance of different driving forces.

The photocatalytic APAP degradation process is based on several simultaneous degradation processes. In order to evaluate the contribution of each degradation mechanism (photolysis without PS, photolysis without catalyst, and pristine catalyst) and their synergistic effect on APAP degradation performance, several experiments had been conducted. According to Fig. 8, the rate constant for pristine catalyst without light, photolysis without PS, and photolysis without catalyst were reported to be 0.0007, 0.0032, 0.0038 min^{-1}, respectively confirmed the low degradability of APAP through these processes. With introduction of these processes and doing an experiment, it has been confirmed that the APAP with decompose rapidly with rate constant of 0.0689 min^{-1}. The results of different experiments, revealed a considerable syn-

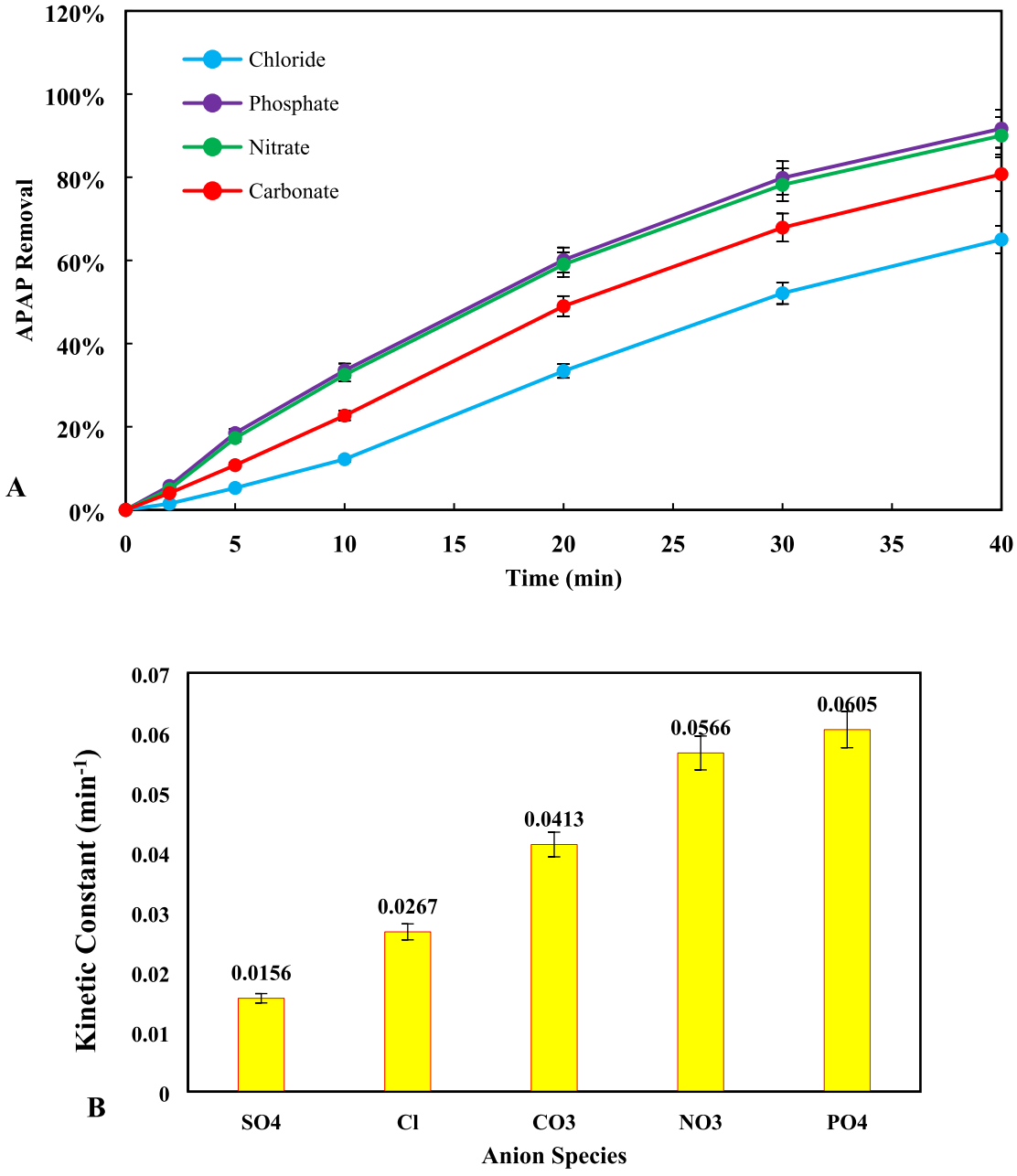

Fig. 10. (A) The role of inorganic anions (NO_3^-, CO_3^{2-}, Cl^- and PO_4^{3-}), (B) the kinetic constant in the photocatalytic process of APAP removal from 0 – 40 min (pH = 11, PS = 1 mM and Fe,Cu@g-C_3N_4 = 10 mg/L).

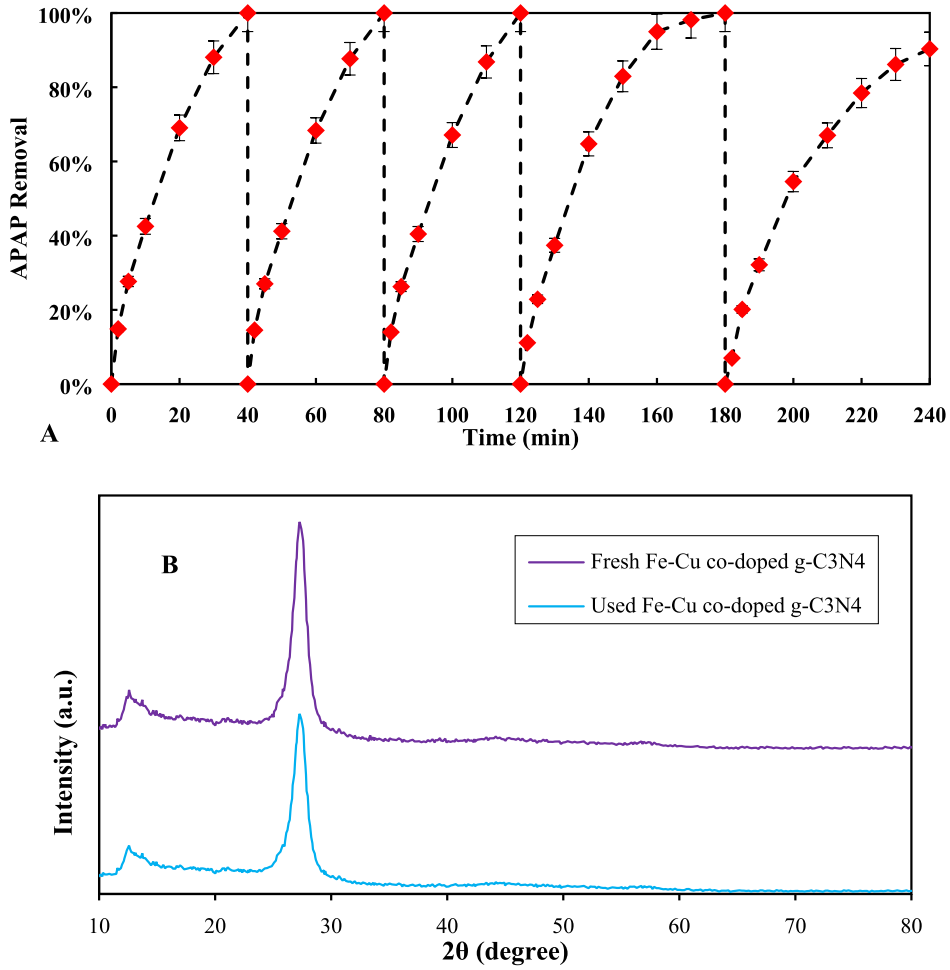

Fig. 11. (A) Stability and reusability of Fe, Cu@g-C_3N_4 during 5 consecutive cycles from 0 to 240 min (pH = 11, PS = 1 mM and Fe,Cu@g-C_3N_4 = 10 mg/L) and (B) XRD patterns of fresh and used Fe, Cu@g-C_3N_4 nanocatalyst.

ergy amongst light irradiation, PS molecules, and catalyst particles by rapid APAP elimination in aquatic medium. In order to evaluate the synergistic factor of final process, following **Eq. (13)** is used:

$$\text{Synergistic factor} = \frac{k_{Cu-Fe@g-C3N4}}{(k_{withoutlight} + k_{withoutpersulfate} + k_{withoutcatalyst})} \quad (13)$$

Where $k_{Fe\text{-}Cu@g\text{-}C3N4}$, $k_{without\ light}$, $k_{without\ PS}$, and $k_{without\ catalyst}$ correspond to rate constants of each process. The synergy factor larger than 1 represents the synergetic effect of processes. However, the synergy factor less than 1 confirm the inhibition effect of processes. For the APAP degradation using light/PS/catalyst system, the synergy factor was found to be 8.9 which prove the considerable synergy of the processes.

3.2.3. Identification of active species in the photocatalytic degradation of APAP

To determine the main oxidizing species or radicals ($O_2^{\cdot -}$, h^+, $HO^{\cdot}$ and $SO_4^{\cdot -}$) responsible for the photocatalytic degradation of APAP pain relievers using Fe,Cu@g-C_3N_4, the several experiments were performed under optimal operating conditions (Hayati, Isari, et al., 2020). The reactions using different deactivating compounds such as disodium ethylenediaminetetraacetic acid (EDTA) as h + scavenger, Ethanol for $HO^{\cdot}$ and $SO_4^{\cdot -}$, p-benzo-quinone (BQ) for $O_2^{\cdot -}$ and Tert-Butyl alcohol (TBA) for $HO^{\cdot}$ at a concentration of 0.01 M. As shown in the Fig. 9, the results show that the removal speed is present in the presence of all active species inactivating agents, and the introduced species participate to different degrees in the photocatalytic removal process of APAP. Apparently, TBA and then Ethanol reduced the amount of removal from 100% to 75.13% and 40.02% respectively in 40 min. The kinetic constant for scavenged reactions were reported to be 0.0665, 0.0197, 0.0304, and 0.0141 min^{-1} for EDTA-Na, ethanol, 1, 4-benzoquinone, and TBA, respectively. The obtained results show

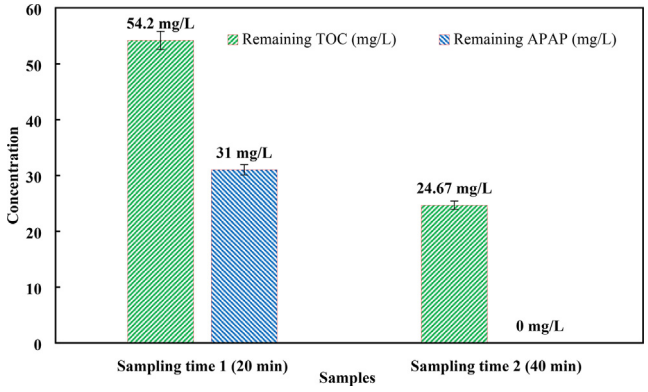

Fig. 12. TOC and APAP Removal under optimal experimental conditions (pH = 11, PS = 1 mM and Fe,Cu@g-C_3N_4 = 10 mg/L).

that in the process of APAP degradation, sulfate radicals play an essential role as the most prominent factor, followed by hydroxyl radicals (Moradi, Isari, et al., 2021).

3.2.4. The role of inorganic anions in the removal process of APAP

In the process of treating wastewater, it is widely recognized that the presence of inorganic anions can have a reductive impact on the effectiveness of catalytic systems in removing target pollutants. Anions can absorb free radicals and generate reactive anionic species, which are often less reactive than hydroxyl and superoxide radicals (Hayati, Isari, et al., 2020). To investigate the impact of inorganic anions on the removal of APAP, 10 mM solutions of Nitrate (NO_3^-), Carbonate (CO_3^{2-}), Chloride (Cl^-) and Phosphate (PO_4^{3-}) were introduced to the reactor under optimal conditions. The inhibitory effect of each anion on the degradation efficiency is shown in Fig. 10 (A and B). It can be observed that all the added anions had an adverse effect on the efficiency of the catalyst in removing APAP. This reduction may be attributed to the anions occupying active sites on the surface of the catalyst, which significantly reduces the number of active sites on the surface and the rate of free radical production. Chloride anion has the most pronounced inhibitory effect on degradation efficiency. This may be due to the formation of chlorine radicals ($Cl_2^{\cdot-}$, $Cl^{\cdot}$ and $ClOH^{\cdot-}$) as shown in **Eqs. S14 to S18**, and the reaction of induced holes and chloride anions, which accelerates the formation of chlorine species. Therefore, the decrease in degradation rate caused by the addition of chloride anions is related to the competition of chloride anions with APAP molecules in consuming active species and/or reacting with hydroxyl and superoxide radicals **Eqs. S19 to S23**.

The addition of nitrate, carbonate, and phosphate anions to the APAP solution resulted in lower removal rates of APAP compared to when no anions were present. This suggests that the inhibitory effects of these anions are not as strong as those of chloride. Nitrate and carbonate anions have less ability to consume hydroxyl radi-

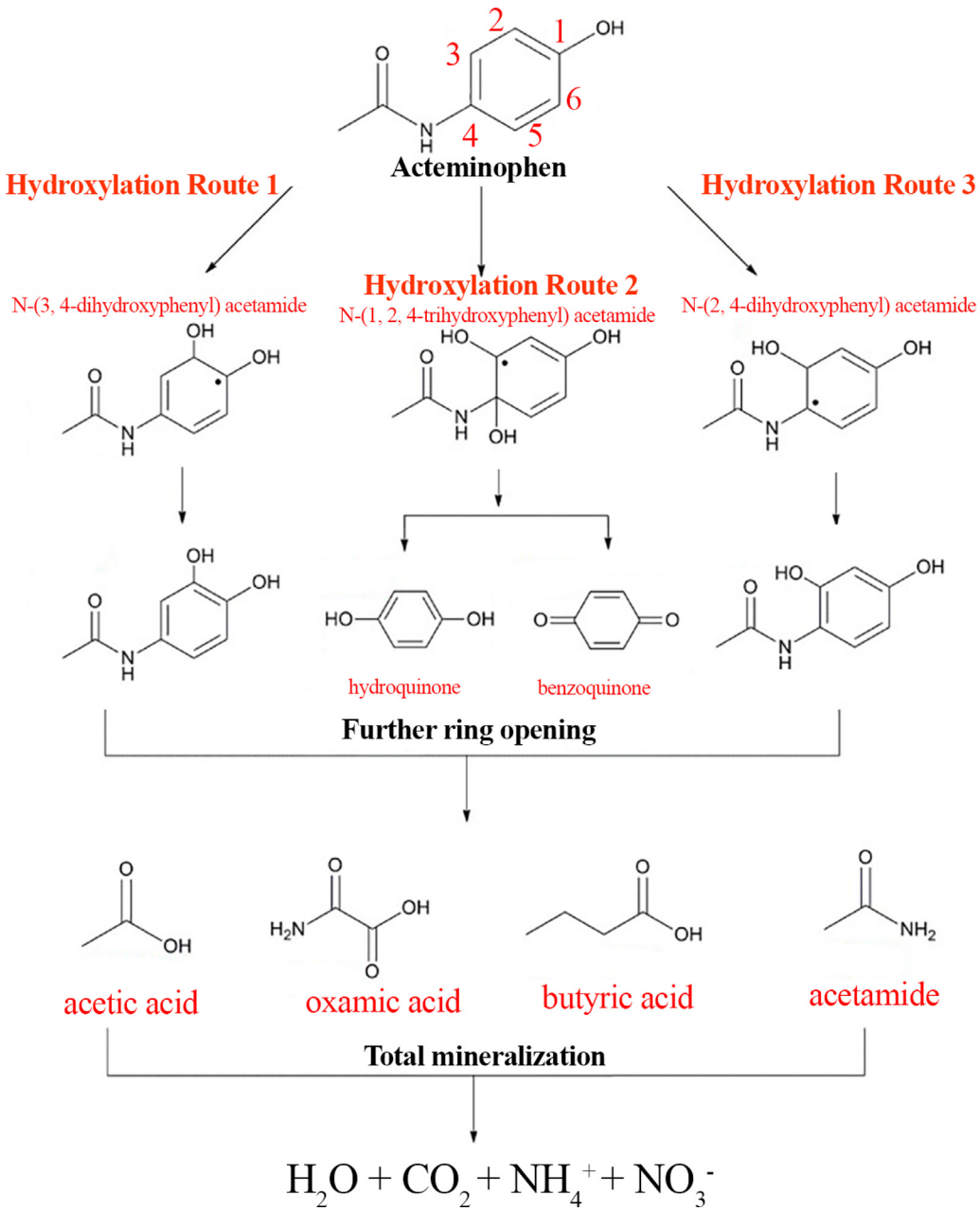

Fig. 13. A plausible pathway for photocatalytic degradation of APAP.

cals and produce NO_3 and CO_3 radicals (**Eqs. S24 and S25**), which may explain why they have weaker inhibitory effects. Additionally, phosphate anions have the least inhibitory effect, likely because they produce PO_4^- radicals at a low rate due to their weak adsorption ability on the nanocomposite surface. **Eq. S20**.

The results also confirmed that anions can significantly reduce the efficiency of the prepared catalyst for APAP removal due to the participation of active species sorbents in the photocatalytic removal reactor through (1) consumption of active species from anions in the path of producing non-radical species, anionic radicals; produced by low oxidation followed by conversion of active species and (3) anions are adsorbed on catalyst surfaces, which reduces the specific surface area and the number of reactive active sites. These findings are highly correlated with the reports of other researchers (Hayati, Isari, et al., 2020; Moradi, Isari, et al., 2021).

3.2.5. Determination of sustainability and reusability of Fe,Cu@g-C_3N_4

In order to evaluate the actual application of the catalyst and its recovery and reuse capability, recovery tests were performed under optimal conditions for APAP removal for 5 consecutive cycles. After each removal test, the used composite was rinsed with diluted hydrochloric acid to remove APAP molecules attached to the catalyst surface. Then, the catalyst was washed using water–ethanol solution (with a volume ratio of 1:1) and dried at 80 °C for 12 hr and used for the next cycle. As shown in Fig. 11**A**, the pollutant removal ability by the synthesized catalyst after 4 removal cycles is still more than 90% of the remaining material, which shows the high stability of this composite in the photocatalytic removal process. In the fifth cycle, the significant reduction in removal efficiency can be due to the reduction of surface active sites, clogging of catalyst pores and reduction of specific surface area, loss of some amount of catalyst in the washing process with acid and water–ethanol, and the loss of surface functional groups on the surface of the catalyst (Deng et al., 2017; Hayati, Khodabakhshi, et al., 2020; A A Isari et al., 2020). After running five consecutive degradation experiments, the XRD analysis of used catalyst were performed and the results are shown in Fig. 11**B.** As can be seen in Fig. 11**B**, the intensity of g-C_3N_4 peaks are reduced. It is confirms that the structure of the used catalyst was not changed during five consecutive decontamination process (S. Chen et al., 2019).

3.2.6. Determining the degree of pollutant (APAP) mineralization

To evaluate the performance of Fe-Cu doped g-C_3N_4 catalyst to break the carbon–carbon bonds in the pollutant, the amount of organic carbon in the sample containing the pollutant was measured at two times 20 min and 40 min after the pollutant removal reaction started, results provided in Fig. 12. In the time of 40 min, the complete removal of APAP pollutant was achieved under optimal operating conditions. At the same time, the amount of 29.53 mg/L of organic carbon in the solution (compared to the amount of organic carbon in 20 min) has been removed. The removal of about 55% of organic carbon in the contaminated sample indicates the high ability of Fe-Cu doped g-C_3N_4 catalyst to break carbon–carbon bonds.

3.2.7. Determination of by-products produced during the removal of APAP

In the process of photocatalytic removal of APAP from the aqueous solution, two samples were taken from the reaction solution at 20 and 40 min after the start of the removal reaction, and chromatographic analysis was performed to identify intermediate substances in the reaction medium. The literature suggests that hydroxylation is the most likely process for breaking down APAP. This means that the C.2, C.3, and C.4 sites of the APAP molecule are the most likely positions for hydroxyl radical (HO•) addition, which can lead to three potential routes for APAP degradation (Fig. 13). Main routes involves the nonselective attack of HO• on C.2 and C.3, resulting in the by-products N-(3, 4-dihydroxyphenyl) acetamide and N-(2, 4-dihydroxyphenyl) acetamide, respectively. Another route involves the addition of HO• onto the aromatic ring at the para position of the –OH group to form hydroquinone. Hydroxylation can also lead to the formation of benzene ring products such as Benzoquinone. Acetic acid, oxamic acid, butyric acid, acetamide could be produced through further oxidation and ring cleavage processes. These products are believed to be biologically inactive and can be removed from water by mineralizing into carbon dioxide and water. Due to the high speed of the elimination reaction and the high ability of hydroxyl and sulfate radicals to attack the bonds in the structure of APAP, intermediate materials or molecular structures are quickly attacked and converted to simpler substances such as phenolic compounds, organic substances with rings opened and even fully mineralized materials such as CO_2, H_2O, NO_3^- and NH_4^+ have been converted. The results obtained are in high agreement with similar studies (Chijioke-Okere et al., 2021; Nasr et al., 2019).

4. Conclusion

In this paper, Cu,Fe co-doped g-C_3N_4 with well-constructed nano-sheet structure was fabricated using thermal decomposition of urea, iron nitrate, and copper nitrate as g-C_3N_4, iron atom and copper atom precursors, respectively. With addition of metal dopants, the same XRD pattern was achieved for both samples, while the BET analysis confirmed the higher specific surface area. The sheet structure of pristine g-C_3N_4 and dopant containing samples were confirmed by SEM micrographs and their purity and uniform atom dispersion were confirmed using EDX and EDX dot mapping analysis, respectively. Under light irradiation, Fe-Cu co-doped g-C_3N_4 nanocomposite showed reduced band gap compared to pristine g-C_3N_4 which confirms the positive effect of addition of metal dopants. Under conditions of pH of 11, catalyst dosage of 10 mg/L, PS dosage of 1 M, and APAP concentration of 4 mg/L, 100% removal of APAP was obtained. The pseudo-first-order kinetic of APAP decomposition with rate constant of 0.0689 min^{-1} was achieved. In investigating the role of scavengers in APAP removal process, it was shown that sulfate and hydroxyl radicals are the main active species in this process. In addition, the results showed that Cu,Fe@g-C_3N_4 had a significant effect in removing TOC and converting organic molecules and 55% TOC reduction was achieved . Therefore, it can be concluded that the present system (PS/-nanocomposite/LED light) was the efficient system to decompose the PPCPs compounds and APAP contain wastewaters.

CRediT authorship contribution statement

Mahtab Alvandi: Methodology, Validation, Formal analysis, Investigation, Data curation. **Heshmatollah Nourmoradi:** Conceptualization, Methodology, Writing – review & editing. **Ali Nikoonahad:** Conceptualization, Methodology, Writing – review & editing. **Ehsan Aghayani:** Methodology, Validation, Formal analysis, Investigation, Data curation, Writing – review & editing. **Seyyed Abbas Mirzaee:** Conceptualization, Methodology, Validation, Resources, Writing – original draft, Writing – review & editing, Project administration.

Declaration of Competing Interest

The authors declare that they have no known competing financial interests or personal relationships that could have appeared to influence the work reported in this paper.

Acknowledgment

This research was extracted from the thesis of Mahtab Alvandi and was financially supported by Ilam University of Medical Sciences (IUMS), Ilam, Iran (grant number: 14014002/11, ID: 1713).

Appendix A. Supplementary material

Supplementary data to this article can be found online at https://doi.org/10.1016/j.arabjc.2023.105251.

References

Adekoya, D.O., Tahir, M., Amin, N.A.S., 2017. g-C3N4/(Cu/TiO2) nanocomposite for enhanced photoreduction of CO2 to CH3OH and HCOOH under UV/visible light. J. CO2 Util. 18, 261–274.

Al Mamari, S., Suliman, F.E., Kim, Y., Selvaraj, R., 2023. Three-dimensional maple leaf CdS/g-C3N4 nanosheet composite for photodegradation of benzene in water. Adv. Powder Technol. 34, (6) 104026.

Anipsitakis, G.P., Dionysiou, D.D., 2004. Transition metal/UV-based advanced oxidation technologies for water decontamination. Appl. Catal. B: Environ. 54 (3), 155–163. https://doi.org/10.1016/j.apcatb.2004.05.025.

Bajiri, M.A., Hezam, A., Keerthiraj, N., Al-Maswari, B.M., Naik, H.S.B., Byrappa, K., Zaqri, N.A., Alsalme, A., Alasmari, R., 2021. Non-noble metallic Cu with three different roles in Cu doped ZnO/Cu/g-C3N4 heterostructure for enhanced Z-scheme photocatalytic activity. New J. Chem.

Chang, J.S., Tan, J.K., Shah, S.N., Mateblowski, A., Strunk, J., Poh, P.E., Chong, M.N., 2017. Morphological tunable three-dimensional flower-like zinc oxides with high photoactivity for targeted environmental Remediation: degradation of emerging micropollutant and radicals trapping experiments. J. Taiwan Inst. Chem. Eng. 81, 206–217.

Chen, L., He, X.-X., Gong, Z.-H., Li, J.-L., Liao, Y., Li, X.-T., Ma, J., 2022. Significantly improved photocatalysis-self-Fenton degradation performance over g-C3N4 via promoting Fe (III)/Fe (II) cycle. Rare Met. 41 (7), 2429–2438.

Chen, S., Li, M., Yang, S., Li, X., Zhang, S., 2019. Graphitied carbon-coated bimetallic FeCu nanoparticles as original g-C3N4 cocatalysts for improving photocatalystic activity. Appl. Surf. Sci. 492, 571–578.

Chen, Y., Liu, K., 2016. Preparation and characterization of nitrogen-doped TiO2/diatomite integrated photocatalytic pellet for the adsorption-degradation of tetracycline hydrochloride using visible light. Chem. Eng. J. 302, 682–696.

Chijioke-Okere, M.O., Hir, Z.A.M., Ogukwe, C.E., Njoku, P.C., Abdullah, A.H., Oguzie, E. E., 2021. TiO2/Polyethersulphone films for photocatalytic degradation of acetaminophen in aqueous solution. J. Mol. Liq. 338, 116692.

Deng, Y., Tang, L., Feng, C., Zeng, G., Wang, J., Lu, Y., Liu, Y., Yu, J., Chen, S., Zhou, Y., 2017. Construction of plasmonic Ag and nitrogen-doped graphene quantum dots codecorated ultrathin graphitic carbon nitride nanosheet composites with enhanced photocatalytic activity: full-spectrum response ability and mechanism insight. ACS Appl. Mater. Interfaces 9 (49), 42816–42828.

Dong, Q., Chen, Y., Wang, L., Ai, S., Ding, H., 2017. Cu-modified alkalinized g-C3N4 as photocatalytically assisted heterogeneous Fenton-like catalyst. Appl. Surf. Sci. 426, 1133–1140.

Duan, X., Sun, H., Wang, S., 2018. Metal-free carbocatalysis in advanced oxidation reactions. Acc. Chem. Res. 51 (3), 678–687.

Fakhri, Y., Nematollahi, A., Bafandeh Tiz, P., Alipour, M., Shahmohammadi, S., Soleymannejad, F., Adiban, M., Khaneghah, A.M., 2022. The concentration of potentially hazardous trace elements (PHTEs) among tap drinking water samples from Ilam city, Iran: A probabilistic non-carcinogenic risk study. Int. J. Environ. Anal. Chem. 102 (17), 5122–5135.

Feng, D., Cheng, Y., He, J., Zheng, L., Shao, D., Wang, W., Wang, W., Lu, F., Dong, H., Liu, H., 2017. Enhanced photocatalytic activities of g-C3N4 with large specific surface area via a facile one-step synthesis process. Carbon 125, 454–463.

Feng, Y., Liao, C., Kong, L., Wu, D., Liu, Y., Lee, P.H., Shih, K., 2018. Facile synthesis of highly reactive and stable Fe-doped g-C3N4 composites for peroxymonosulfate activation: A novel nonradical oxidation process. J. Hazard. Mater. 354 (January), 63–71. https://doi.org/10.1016/j.jhazmat.2018.04.056.

Ghanbari, F., Moradi, M., Manshouri, M., 2014. Textile wastewater decolorization by zero valent iron activated peroxymonosulfate: Compared with zero valent copper. J. Environ. Chem. Eng. 2 (3), 1846–1851. https://doi.org/10.1016/j.jece.2014.08.003.

Ghanbari, F., Giannakis, S., Lin, K.-Y.-A., Wu, J., Madihi-Bidgoli, S., 2021. Acetaminophen degradation by a synergistic peracetic acid/UVC-LED/Fe (II) advanced oxidation process: Kinetic assessment, process feasibility and mechanistic considerations. Chemosphere 263, 128119.

Ghane, N., Sadrnezhaad, S. K., & H, S. M. H. (2020). Applied Surface Science Combustion synthesis of g-C 3 N 4 / Fe 2 O 3 nanocomposite for superior photoelectrochemical catalytic performance. 534(May).

Han, W., Li, D., Zhang, M., Ximin, H., Duan, X., Liu, S., Wang, S., 2020. Photocatalytic activation of peroxymonosulfate by surface-tailored carbon quantum dots. J. Hazard. Mater. 395, 122695.

Hassani, A., Eghbali, P., Kakavandi, B., Lin, K.Y.A., Ghanbari, F., 2020. Acetaminophen removal from aqueous solutions through peroxymonosulfate activation by CoFe2O4/mpg-C3N4 nanocomposite: Insight into the performance and degradation kinetics. Environ. Technol. Innov. 20. https://doi.org/10.1016/j.eti.2020.101127.

Hayati, F., Isari, A.A., Anvaripour, B., Fattahi, M., Kakavandi, B., 2020. Ultrasound-assisted photocatalytic degradation of sulfadiazine using MgO@ CNT heterojunction composite: effective factors, pathway and biodegradability studies. Chem. Eng. J. 381, 122636.

Hayati, F., Khodabakhshi, M.R., Isari, A.A., Moradi, S., Kakavandi, B., 2020. LED-assisted sonocatalysis of sulfathiazole and pharmaceutical wastewater using N, Fe co-doped TiO2@ SWCNT: Optimization, performance and reaction mechanism studies. J. Water Process Eng. 38, 101693.

Hu, S., Li, F., Fan, Z., Wang, F., Zhao, Y., Lv, Z., 2015. Band gap-tunable potassium doped graphitic carbon nitride with enhanced mineralization ability. Dalton Trans. 44 (3), 1084–1092.

Hu, S., Chen, X., Li, Q., Zhao, Y., Mao, W., 2016. Effect of sulfur vacancies on the nitrogen photofixation performance of ternary metal sulfide photocatalysts. Cat. Sci. Technol. 6 (15), 5884–5890.

Hu, S., Chen, X., Li, Q., Li, F., Fan, Z., Wang, H., Wang, Y., Zheng, B., Wu, G., 2017. Fe3+ doping promoted N2 photofixation ability of honeycombed graphitic carbon nitride: The experimental and density functional theory simulation analysis. Appl. Catal. B: Environ. 201, 58–69.

Hu, S., Qu, X., Bai, J., Li, P., Li, Q., Wang, F., Song, L., 2017. Effect of Cu (I)–N active sites on the N2 photofixation ability over flowerlike copper-doped g-C3N4 prepared via a novel molten salt-assisted microwave process: the experimental and density functional theory simulation analysis. ACS Sustain. Chem. Eng. 5 (8), 6863–6872.

Hu, S., Qu, X., Li, P., Wang, F., Li, Q., Song, L., Zhao, Y., Kang, X., 2018. Photocatalytic oxygen reduction to hydrogen peroxide over copper doped graphitic carbon nitride hollow microsphere: the effect of Cu (I)-N active sites. Chem. Eng. J. 334, 410–418.

Hu, J., Tian, K., Jiang, H., 2016. Chemosphere Improvement of phenol photodegradation ef fi ciency by a combined g- C 3 N 4 / Fe (III)/ persulfate system. Chemosphere 148, 34–40. https://doi.org/10.1016/j.chemosphere.2016.01.002.

Isari, A.A., Hayati, F., Kakavandi, B., Rostami, M., Motevassel, M., Dehghanifard, E., 2020. N, Cu co-doped TiO2@ functionalized SWCNT photocatalyst coupled with ultrasound and visible-light: an effective sono-photocatalysis process for pharmaceutical wastewaters treatment. Chem. Eng. J. 392, 123685.

Jaafarzadeh, N., Baboli, Z., Noorimotlagh, Z., Martínez, S.S., Ahmadi, M., Alavi, S., Mirzaee, S., 2019. Efficient adsorption of bisphenol A from aqueous solutions using low-cost activated carbons produced from natural and synthetic carbonaceous materials. Desalin. Water Treat. 154, 177–187.

Kakavandi, B., Bahari, N., Rezaei Kalantary, R., Dehghani Fard, E., 2019. Enhanced sono-photocatalysis of tetracycline antibiotic using TiO2 decorated on magnetic activated carbon (MAC@T) coupled with US and UV: A new hybrid system. Ultrason. Sonochem. 55, 75–85. https://doi.org/10.1016/j.ultsonch.2019.02.026.

Keerthanan, S., Jayasinghe, C., Biswas, J.K., Vithanage, M., 2021. Pharmaceutical and Personal Care Products (PPCPs) in the environment: Plant uptake, translocation, bioaccumulation, and human health risks. Crit. Rev. Environ. Sci. Technol. 51 (12), 1221–1258. https://doi.org/10.1080/10643389.2020.1753634.

Kim, Y., Choi, K., Jung, J., Park, S., Kim, P.G., Park, J., 2007. Aquatic toxicity of acetaminophen, carbamazepine, cimetidine, diltiazem and six major sulfonamides, and their potential ecological risks in Korea. Environ. Int. 33 (3), 370–375. https://doi.org/10.1016/j.envint.2006.11.017.

Kohantorabi, M., Moussavi, G., Oulego, P., Giannakis, S., 2022. Deriving an α-Fe2O3/g-C3N4 nanocomposite from a naturally hematite-rich soil, for dual photocatalytic and photo-Fenton degradation of Acetaminophen under visible light. Sep. Purif. Technol. 299, 121723.

Li, K., Gao, S., Wang, Q., Xu, H., Wang, Z., Huang, B., Dai, Y., & Lu, J. (2015). *In Situ Reduced Synthesis of Ti3 + Self-Doped TiO2 / g-C3N4 Heterojunctions with High Photocatalytic Performance under LED Light Irradiation*. doi: 10.1021/am508505n.

Li, R., Huang, J., Cai, M., Huang, J., Xie, Z., Zhang, Q., Liu, Y., Liu, H., Lv, W., Liu, G., 2020. Activation of peroxymonosulfate by Fe doped g-C3N4 /graphene under visible light irradiation for Trimethoprim degradation. J. Hazard. Mater. 384 (July). https://doi.org/10.1016/j.jhazmat.2019.121435.

Li, Y., Jindal, R., Choi, K., Kho, Y.L., de Bullen, P.G., 2012. Pharmaceutical residues in wastewater treatment plants and surface waters in Bangkok. J. Hazard. Toxic Radioact. Waste 16 (1), 88–91. https://doi.org/10.1061/(asce)hz.2153-5515.0000099.

Li, Z., Kong, C., Lu, G., 2016. Visible photocatalytic water splitting and photocatalytic two-electron oxygen formation over Cu-and Fe-doped g-C3N4. J. Phys. Chem. C 120 (1), 56–63.

Li, Y., Li, S., Chao, C., Yao, S., Zhang, D., Chen, Q., 2022. Enhanced visible-light activation of persulfate by g-C3N4 decorated graphene aerogel for methyl orange degradation. J. Alloy. Compd. 926, 166904.

Li, D., Liu, H., Niu, C., Yuan, J., Xu, F., 2019. Mpg-C3N4-ZIF-8 composites for the degradation of tetracycline hydrochloride using visible light. Water Sci. Technol. 80 (11), 2206–2217.

Li, D., Yang, J., Lv, S., Li, X., Shao, L., Zhou, C., Xu, F., 2023. Insights into the degradation mechanisms of TCH by magnetic Fe3S4/Cu2O composite. Inorg. Chem. 62 (27), 10713–10726.

Lin, H., Wu, J., Zhang, H., 2013. Degradation of bisphenol A in aqueous solution by a novel electro / Fe 3 + / peroxydisulfate process. Sep. Purif. Technol. 117, 18–23. https://doi.org/10.1016/j.seppur.2013.04.026.

Liu, B., Qiao, M., Wang, Y., Wang, L., Gong, Y., Guo, T., Zhao, X., 2017. Persulfate enhanced photocatalytic degradation of bisphenol A by g-C3N4 nanosheets under visible light irradiation. Chemosphere 189, 115–122. https://doi.org/10.1016/j.chemosphere.2017.08.169.

Ma, T., Shen, Q., Zhaoa, B., Xue, J., Guan, R., Liu, X., Jia, H., Xu, B., 2019. Facile synthesis of Fe-doped g-C3N4 for enhanced visible-light photocatalytic activity. Inorg. Chem. Commun. 107, 107451.

Mehregan, S., Hayati, F., Mehregan, M., Isari, A.A., Jonidi Jafari, A., Giannakis, S., Kakavandi, B., 2022. Exploring the visible light–assisted conversion of CO2 into methane and methanol, using direct Z-scheme TiO2@ g-C3N4 nanosheets: synthesis and photocatalytic performance. Environ. Sci. Pollut. Res. 29 (49), 74951–74966.

Mirzaee, S. A., N. Jaafarzadeh, H. T. Gomes, S. Jorfi and M. Ahmadi (2019)b. "Magnetic titanium/carbon nanotube nanocomposite catalyst for oxidative degradation of Bisphenol A from high saline polycarbonate plant effluent using catalytic wet peroxide oxidation." Chemical Engineering Journal 370: 372-386.

Mirzaee, S. A., Noorimotlagh, Z., Ahmadi, M., Rahim, F., Martinez, S. S., Nourmohammadi, A., & Jaafarzadeh, N. (2021)a. The possible oxidative stress and DNA damage induced in Diclofenac-exposed Non-target organisms in the aquatic environment: A systematic review. Ecological Indicators, 131, 108172. doi:https://doi.org/10.1016/j.ecolind.2021.108172.

Moradi, S., Isari, A.A., Hayati, F., Kalantary, R.R., Kakavandi, B., 2021. Co-implanting of TiO2 and liquid-phase-delaminated g-C3N4 on multi-functional graphene nanobridges for enhancing photocatalytic degradation of acetaminophen. Chem. Eng. J. 414, 128618.

Nasr, O., Mohamed, O., Al-Shirbini, A.-S., Abdel-Wahab, A.-M., 2019. Photocatalytic degradation of acetaminophen over Ag, Au and Pt loaded TiO2 using solar light. J. Photochem. Photobiol. A Chem. 374, 185–193.

Noorimotlagh, Z., Darvishi Cheshmeh Soltani, R., Shams Khorramabadi, G., Godini, H., & Almasian, M. (2016)a. Performance of wastewater sludge modified with zinc oxide nanoparticles in the removal of methylene blue from aqueous solutions. . Desalination and Water Treatment, 57(4), 1684-1692. doi: https://doi.org/10.1080/19443994.2014.977954.

Noorimotlagh, Z., Dehvari, M., Mirzaee, S. A., Jaafarzadeh, N., Martínez, S. S., & Amarloei, A. (2023)b. Efficient sonocatalytic degradation of orange II dye and real textile wastewater using peroxymonosulfate activated with a novel heterogeneous TiO2–FeZn bimetallic nanocatalyst. Journal of the Iranian Chemical Society, 20(7), 1589-1603. doi:10.1007/s13738-023-02780-3.

Ong, W.J., Tan, L.L., Chai, S.P., Yong, S.T., Mohamed, A.R., 2015. Surface charge modification via protonation of graphitic carbon nitride (g-C3N4) for electrostatic self-assembly construction of 2D/2D reduced graphene oxide (rGO)/g-C3N4 nanostructures toward enhanced photocatalytic reduction of carbon dioxide to methane. Nano Energy 13, 757–770. https://doi.org/10.1016/j.nanoen.2015.03.014.

Pan, G., & Sun, Z. (2021a). *Chemosphere Cu-doped g-C 3 N 4 catalyst with stable Cu 0 and Cu + for enhanced amoxicillin degradation by heterogeneous electro-Fenton process at neutral pH*. *283*(June).

Pan, G., Sun, Z., 2021b. Cu-doped g-C3N4 catalyst with stable Cu0 and Cu+ for enhanced amoxicillin degradation by heterogeneous electro-Fenton process at neutral pH. Chemosphere 283 (June). https://doi.org/10.1016/j.chemosphere.2021.131257.

Qin, S., Liu, Y., Liu, S., Wang, X., Li, Y., Qin, C., Wang, Z., Li, M., 2022. Self-standing porous Au/CuO nanowires with remarkably enhanced visible light absorption and photocatalytic performance. Appl. Surf. Sci. 594, 153443.

Ruppert, G., Bauer, R., Heisler, G., 1994. UV-O3, UV-H2O2, UV-TiO2 and the photo-Fenton reaction-comparison of advanced oxidation processes for wastewater treatment. Chemosphere 28 (8), 1447–1454.

Sarkar, S., Sumukh, S.S., Roy, K., Kamboj, N., Purkait, T., Das, M., Dey, R.S., 2020. Facile one step synthesis of Cu-g-C3N4 electrocatalyst realized oxygen reduction reaction with excellent methanol crossover impact and durability. J. Colloid Interface Sci. 558, 182–189.

Shi, W., Hao, C., Fu, Y., Guo, F., Tang, Y., Yan, X., 2022. Enhancement of synergistic effect photocatalytic/persulfate activation for degradation of antibiotics by the combination of photo-induced electrons and carbon dots. Chem. Eng. J. 433, 133741.

Sim, W.J., Lee, J.W., Oh, J.E., 2010. Occurrence and fate of pharmaceuticals in wastewater treatment plants and rivers in Korea. Environ. Pollut. 158 (5), 1938–1947. https://doi.org/10.1016/j.envpol.2009.10.036.

Takdastan, A., Kakavandi, B., Azizi, M., Golshan, M., 2018. Efficient activation of peroxymonosulfate by using ferroferric oxide supported on carbon/UV/US system: a new approach into catalytic degradation of bisphenol A. Chem. Eng. J. 331, 729–743.

Tan, C., Gao, N., Fu, D., Deng, J., Deng, L., 2017. Efficient degradation of paracetamol with nanoscaled magnetic CoFe2O4 and MnFe2O4 as a heterogeneous catalyst of peroxymonosulfate. Sep. Purif. Technol. 175, 47–57.

Wang, S., Long, J., Jiang, T., Shao, L., Li, D., Xie, X., Xu, F., 2021. Magnetic Fe3O4/CeO2/g-C3N4 composites with a visible-light response as a high efficiency Fenton photocatalyst to synergistically degrade tetracycline. Sep. Purif. Technol. 278, 119609.

Wang, J., Wang, S., 2018. Activation of persulfate (PS) and peroxymonosulfate (PMS) and application for the degradation of emerging contaminants. Chem. Eng. J. 334, 1502–1517.

Wang, S., Wu, J., Lu, X., Xu, W., Gong, Q., Ding, J., Dan, B., Xie, P., 2019. Removal of acetaminophen in the Fe2+/persulfate system: Kinetic model and degradation pathways. Chem. Eng. J. 358, 1091–1100. https://doi.org/10.1016/j.cej.2018.09.145.

Yang, L., Bai, X., Shi, J., Du, X., Xu, L., Jin, P., 2019. Quasi-full-visible-light absorption by D35-TiO2/g-C3N4 for synergistic persulfate activation towards efficient photodegradation of micropollutants. Appl. Catal. B: Environ. 256. https://doi.org/10.1016/j.apcatb.2019.117759.

Yang, X., Cao, C., Erickson, L., Hohn, K., Maghirang, R., Klabunde, K., 2008. Synthesis of visible-light-active TiO2-based photocatalysts by carbon and nitrogen doping. J. Catal. 260 (1), 128–133. https://doi.org/10.1016/j.jcat.2008.09.016.

Yang, X., Cao, X., Tang, B., Shan, B., Deng, M., Liu, Y., 2019. rGO/Fe-doped g-C3N4 visible-light driven photocatalyst with improved NO removal performance. J. Photochem. Photobiol. A Chem. 375, 40–47.

Yang, L., Ren, X., Zhang, Y., Chen, Z., Wan, J., 2021. One-step synthesis of a heterogeneous catalyst: Cu+-decorated triazine-based g-C3N4 nanosheet formation and catalytic mechanism. J. Environ. Chem. Eng. 9, (4) 105558.

Yuan, J., Zhou, H., Li, D., Xu, F., 2023. Construction of Fe3S4/g-C3N4 composites as photo-Fenton-like catalysts to realize high-efficiency degradation of pollutants. Ceram. Int. 49 (10), 16070–16079.

Zhang, L., Li, B., Xu, H.-Y., 2022. Visible-light-driven peroxydisulfate activation by BiOI/g-C3N4 heterojunction for high-concentration dyes degradation: A comprehensive study. J. Mater. Res. 37 (12), 2093–2107.

Zhang, J., Zhang, M., Lin, S., Fu, X., Wang, X., 2014. Molecular doping of carbon nitride photocatalysts with tunable bandgap and enhanced activity. J. Catal. 310, 24–30. https://doi.org/10.1016/j.jcat.2013.01.008.

Zhao, J., Ma, L., Wang, H., Zhao, Y., Zhang, J., Hu, S., 2015. Novel band gap-tunable K-Na co-doped graphitic carbon nitride prepared by molten salt method. Appl. Surf. Sci. 332, 625–630.

Zhou, H., Wang, S., Jiang, J., Shao, L., Li, D., Yuan, J., Xu, F., 2022. Magnetic Fe3S4/MoS2 with visible-light response as an efficient photo-Fenton-like catalyst: Validation in degrading tetracycline hydrochloride under mild pH conditions. J. Alloy. Compd. 921, 166023.

Zhu, Z., Huo, P., Lu, Z., Yan, Y., Liu, Z., Shi, W., Li, C., Dong, H., 2018. Fabrication of magnetically recoverable photocatalysts using g-C3N4 for effective separation of charge carriers through like-Z-scheme mechanism with Fe3O4 mediator. Chem. Eng. J. 331, 615–625.

Zou, Y., Kang, S.Z., Li, X., Qin, L., Mu, J., 2014. TiO2 nanosheets loaded with Cu: A low-cost efficient photocatalytic system for hydrogen evolution from water. Int. J. Hydrogen Energy 39 (28), 15403–15410. https://doi.org/10.1016/j.ijhydene.2014.07.174.